

# Formation mechanism of abnormally large grains in a polycrystalline nickel-based superalloy during heat treatment processing

Wang, Xin; Huang, Zaiwang; Cai, Biao; Zhou, Ning; Magdysyuk, Oxana; Gao, Yanfei; Srivatsa, Shesh; Tan, Liming; Jiang, Liang

DOI:

[10.1016/j.actamat.2019.02.012](https://doi.org/10.1016/j.actamat.2019.02.012)

License:

Creative Commons: Attribution-NonCommercial-NoDerivs (CC BY-NC-ND)

*Document Version*

Peer reviewed version

*Citation for published version (Harvard):*

Wang, X, Huang, Z, Cai, B, Zhou, N, Magdysyuk, O, Gao, Y, Srivatsa, S, Tan, L & Jiang, L 2019, 'Formation mechanism of abnormally large grains in a polycrystalline nickel-based superalloy during heat treatment processing', *Acta Materialia*, vol. 168, pp. 287-298. <https://doi.org/10.1016/j.actamat.2019.02.012>

[Link to publication on Research at Birmingham portal](#)

## **Publisher Rights Statement:**

Checked for eligibility: 13/03/2019

## **General rights**

Unless a licence is specified above, all rights (including copyright and moral rights) in this document are retained by the authors and/or the copyright holders. The express permission of the copyright holder must be obtained for any use of this material other than for purposes permitted by law.

- Users may freely distribute the URL that is used to identify this publication.
- Users may download and/or print one copy of the publication from the University of Birmingham research portal for the purpose of private study or non-commercial research.
- User may use extracts from the document in line with the concept of 'fair dealing' under the Copyright, Designs and Patents Act 1988 (?)
- Users may not further distribute the material nor use it for the purposes of commercial gain.

Where a licence is displayed above, please note the terms and conditions of the licence govern your use of this document.

When citing, please reference the published version.

## **Take down policy**

While the University of Birmingham exercises care and attention in making items available there are rare occasions when an item has been uploaded in error or has been deemed to be commercially or otherwise sensitive.

If you believe that this is the case for this document, please contact [UBIRA@lists.bham.ac.uk](mailto:UBIRA@lists.bham.ac.uk) providing details and we will remove access to the work immediately and investigate.

Formation Mechanism of Abnormally Large Grains in a Polycrystalline Nickel-based Superalloy during Heat Treatment Processing

Xin Wang<sup>a</sup>, Zaiwang Huang<sup>a\*</sup>, Biao Cai<sup>b\*\*</sup>, Ning Zhou<sup>c</sup>, Oxana Magdysyuk<sup>d</sup>, Yanfei Gao<sup>e</sup>, Shesh Srivatsa<sup>f</sup>, Liming Tan<sup>a</sup>, Liang Jiang<sup>a</sup>

- a. State Key Laboratory of Powder Metallurgy, Central South University, Changsha, 410083, PR China  
Email: xin.wang.418@gmail.com (Xin Wang), huangzaiwang@csu.edu.cn (Zaiwang Huang), limingtan@csu.edu.cn (Liming Tan), liang.jiang@csu.edu.cn (Liang Jiang)
- b. School of Metallurgy and Materials, University of Birmingham, Edgbaston Birmingham B15 2TT, UK  
Email: b.cai@bham.ac.uk
- c. Clifton Park, New York 12065, USA  
Email: zhouning1978@gmail.com
- d. Diamond Light Source Ltd, Harwell Science and Innovation Campus, Didcot OX11 0DE, UK.  
Email: oxana.magdysyuk@diamond.ac.uk
- e. Department of Materials Science and Engineering, University of Tennessee, Knoxville, Tennessee 37996, USA  
Email: ygao7@utk.edu
- f. Srivatsa Consulting LLC, 8190 Glenmill Ct, Cincinnati, OH 45249, USA  
Email: shesh.srivatsa@gmail.com

**Abstract:**

Controlling the final grain size in a uniform and controlled manner in powder metallurgy nickel-based superalloys is important since many mechanical properties are closely related to it. However, it has been widely documented that powder metallurgy superalloys are prone to suffer from growth of abnormally large grains (ALGs) during supersolvus heat treatment, which is harmful to in-service mechanical performance. The underlying mechanisms behind the formation of ALGs are not yet fully understood. In this research, ALGs were intentionally created using spherical indentation applied to a polycrystalline nickel-based superalloy at room temperature, establishing a deformation gradient underneath the indentation impression, which was quantitatively determined using finite element modelling, electron backscatter diffraction (EBSD) and synchrotron diffraction. Subsequent supersolvus heat treatment leads to the formation of ALGs in a narrow strain range, which also coincides with the contour of residual plastic strain in a range of about 2% to 10%. The formation mechanisms can be attributed to: (1) nucleation sites available for recrystallization are limited, (2) gradient distribution of stored energy across grain boundary. The proposed mechanisms were validated by the phase-field simulation. This research provides a deeper insight in understanding the formation of ALGs in polycrystalline nickel-based superalloy components during heat treatment, when subsurface plastic deformation caused by (mis)handling before super-solvus heat treatment occurs. The practical relevance of looking at small strains at room temperature this research is to understand what happens when turbine disks undergo small dents and scratches during (mis) handling before heat treatment.

**Keywords:**

Nickel-based superalloys, Abnormal grain growth, Local strain distribution, Dislocation density, Phase field modeling

## **Introduction**

Powder metallurgy nickel-based superalloys have been widely used in gas turbine disks due to their good mechanical strength, creep and fatigue crack growth resistance at elevated temperatures. These attractive high temperature mechanical properties are primarily attributed to a synergetic strengthening effect of desirable grain size and precipitate microstructure [1]. Particularly, critical mechanical properties are governed by grain size distribution [2]. For instance, low cycle fatigue life and tensile strength increase with smaller grain size as compared to creep strength and fatigue crack growth rate which decreases with smaller grain size. Typically, after a series of thermo-mechanical processing steps, supersolvus heat treatment is performed in a controlled manner in order to uniformly coarsen the grains, targeting to improve fatigue crack growth resistance and creep strength. Tuning grain size into optimal distribution during supersolvus heat treatment is crucial, for the reason that the grain size requirement is application-oriented. It has been well documented that abnormally large grains (ALGs) are prone to be triggered in forged nickel base superalloys containing a critical window of strain or strain rate during supersolvus heat treatment, leading to a bimodal grain size distribution [3]. The unexpected occurrence of localized ALGs will cause microstructural inhomogeneity and degrade the structural integrity (e.g. previous studies [4,5] show ALGs could act as initiation sites for fatigue cracks). It can also cause conventional models [6] to fail to predict the grain structure after heat treatment.

Different terminologies have been used to report this ALG phenomenon, such as abnormal grain growth (AGG) and critical grain growth (CGG). In the classical AGG theory, a few local grains that have favorable growth conditions may grow excessively when normal grain growth (NGG) is inhibited, e.g. by second-phase particles [7], texture [8] or boundary

anisotropy [9]. The driving force of AGG comes from the reduction of grain boundary area, similar to NGG [6,10]. It should be noted that AGG models and theories [11–15] are not explicitly connected to the prior deformation. Different from AGG theories, CGG is developed to describe the dramatic grain growth leading to the formation of ALGs if the alloy is deformed within a small window of critical strain at room temperature [16]. In the case of high temperature deformation, critical strain rate at given temperature is considered as a more practical indicator for the onset of CGG instead of strain [17], since deformation mechanisms at high temperatures are solely determined by strain rate and temperature.

To prevent the occurrence of ALGs, many ad hoc studies [3,18–29] have been conducted to find the critical window of strain and/or strain rate. For example, it has been found that nominal compressive strain below 10% could trigger the occurrence of ALGs after supersolvus heat treatment [19]. The critical strain window depends on the alloy composition, preparation condition [23] and heat treatment profile [22]. Based on these experimental observations, two competing mechanisms are developed and are now widely accepted:

Heterogeneity of stored energy distribution at the grain scale. Agnoli et al. [26,30] reported the stored energy heterogeneity using level-set simulation and experiment and argued that strain-induced selective grain growth was responsible for the formation of ALGs, which involves the excessive growth of a few lower stored energy grains at the expense of grains with higher stored energy. This heterogeneous stored energy distribution in grain scale was also observed in forged nickel base superalloys [31–33].

Nucleation sites limited recrystallization. It is well established that recrystallization could take place during annealing if the stored energy level exceeds a threshold at a given temperature [6]. The stored energy provides the driving force available for recrystallization. Lowering driving force statistically results in fewer recrystallization grains that nucleate and grow via consuming neighboring matrix. This process was confirmed by the experimental

observations [34] that final grain size is inversely related with prior deformation level after annealing. Miller et al. [3] argued that the growth of ALGs is this kind of ‘abnormal’ recrystallization process rather than driven by AGG mechanism alone based on the fact that growth rate of ALGs front is an order of magnitude higher than that in previously reported AGG experiments.

To date, however, the quantitative nature of the above competing mechanisms is not fully understood, and the precise knowledge of how much deformation is needed to trigger ALGs formation is unknown from previous investigations. In this paper, we use a spherical indentation to generate a deformation gradient at room temperature so that the deformation-dependent grain growth behavior can be correlated to the amount of strain applied. This old technique has been used before to study strain-related phenomenon[35]. Both experimentation and simulation tools are employed to assess the extent of deformation and full dislocation density distribution after indentation. Indented samples were subjected to different heat treatment procedures and the onset condition for ALGs was determined. The results clearly demonstrate that the formation of ALGs is driven by stored energy related mechanism as demonstrated also by phase field simulation.

Although extreme care is taken in the processing and handling of superalloy aerospace components, very rarely small dents and scratches could occur during handling before heat treatment. The practical relevance of looking at small strains at room temperature is to understand what happens when this type of subsurface plastic deformation caused by (mis)handling occurs. turbine disks undergo small dents and scratches during (mis) handling before heat treatment.

## 2. Experimental

### 2.1. Materials

The nickel-based superalloy used in this study had a nominal composition Ni-13Co-

16Cr-4Mo-4W-2.1Al-3.1Ti-0.7Nb-0.015B-0.03Zr-0.03C (in weight percentage) [36]. The powder was produced by argon atomization process and sieved to obtain a maximum powder particle size 74  $\mu\text{m}$ . The sieved powder was filled into a mild steel container followed by de-gassing and sealing. Hot isostatic pressing (HIP) consolidation was performed at 150 MPa and 1120 °C for 4 hours. The HIPed container was hot-extruded at 1070 °C using an extrusion ratio of 4:1.

Cylindrical samples with a height 9 mm and diameter 10 mm were sectioned from the HIPed billet using electrical discharge machining (EDM). The axis of all the cylindrical samples was parallel to the extrusion direction.

## **2.2. Indentation experiment**

The indentation tests were performed on an MTS Landmark 370 servo-hydraulic test system using a specially designed fixture equipped with a 5 mm diameter tungsten carbide ball indenter. Before indentation, the surface to be indented was slightly ground to remove the EDM recast layer and then polished using 0.3  $\mu\text{m}$  alumina suspension. The initial contact between indenter and sample was made by setting a 0.5 KN preload at a speed of 5 mm/min. Indentation ramp was set to end at 15 KN with a ramp rate of 15 KN/min, and dwell for 20 s. Instant unloading was done using displacement control mode.

## **2.3. Heat treatment**

All the indented samples were sealed in fused silica and backfilled with argon before heat treatment. The  $\gamma'$  solvus temperature was determined to be 1107 °C by thermodynamic calculation using the Thermo-Calc package with TTNi8 database (see Supplementary data A). The heat treatment temperatures were set to be 1080 °C and 1150 °C, which corresponds to subsolvus and supersolvus solution heat treatment for this material respectively. Heat treatment was carried out in a box furnace (CM Furnaces Inc., 1610 BL), the heating ramp rate was set

to be 10 °C per minute. One type B thermocouple (Pt/30%Rh–Pt/6%Rh, by weight) was used to measure and control the temperature.

In addition, a short time heat treatment was also conducted at 1150 °C using induction heating, in order to investigate the initiation of abnormally large grains. The frequency of power supply for the induction coil was 200 KHz, and it took approximately 35 seconds to heat the sample from room temperature to the set-point temperature. The temperature was measured and controlled by a type S thermocouple (Pt/10%Rh–Pt, by weight) welded on the sample. After holding at 1150 °C for 30 seconds, the sample was quenched with compressed air.

#### **2.4. Microstructure characterization**

Two planes are of interest in this investigation: indented plane and section plane, which are perpendicular and parallel to the indentation direction respectively. Samples of the section plane were prepared by cutting through the center of the indentation impression. (see Supplementary data B)

Standard metallographic procedures were used for preparing samples for microstructure observation under the guideline of ASTM E3-11 standard. An additional vibratory polishing in 0.05 µm colloidal silica was employed for electron backscatter diffraction (EBSD) samples. Optical micrographs were obtained on Leica DM4000 M, and electron imaging was performed on the FEI Quanta FEG 650 scanning electron microscope, in which EBSD experiment was carried out using an EBSD detector (Oxford Instrument plc, NordlysMax2) with a 640×480 resolution charge-coupled device (CCD) and AZtec software. During data acquisition, the CCD was binned to 320 × 240 or 160 × 120, by considering both time consumption and accuracy, and the accuracy was assured by the fact that the average mean angular deviations of all EBSD data were under 0.8°. Various step sizes were used depending on magnifications. HKL Channel 5 package was used for post-analyzing the EBSD data. The average grain size measurement was done by analyzing EBSD data following ASTM E2627-13 standard, the fraction of



modified data in cleanup routine was no more than 10%. The largest grain size was directly obtained from the grain list output.

## 2.5 Synchrotron diffraction

Synchrotron high energy X-ray diffraction was conducted on the I12 beamline at the Diamond Light Source in UK with X-ray energy of 80 keV and beam size of 50  $\mu\text{m}$ . The RF Pixium 4343 2D area detector with a pixel size of 148  $\mu\text{m} \times 148 \mu\text{m}$  on a 2880  $\times$  2881 X-ray sensitive array was used in transmission mode. The sample was positioned 800 mm away from the detector. The CeO<sub>2</sub> was used to perform the calibration. A thin plate with thickness of 1 mm was cut along the central section plane from the indented sample. The 50  $\mu\text{m}$  X-ray was used to map the region underneath the indentation impression with a step size of 50  $\mu\text{m}$ .

## 2.6. Diffraction profile analysis

To quantitatively analyze the dislocation density in the sample after spherical indentation, the dislocation density was estimated from the synchrotron diffraction profile. Williamson and Hall [37] suggest that the broadening of diffraction line profile  $\Delta K$  is due to the combined effect of strain and grain size and can be written as [38]:

$$\Delta K = \frac{0.9}{D} + \Delta K^D, (1)$$

where  $\Delta K^D$  and  $0.9/D$  ( $D$  represents grain size) are the strain and grain size contribution respectively.  $K = 2\sin\theta/\lambda$ ,  $\Delta K = 2\cos\theta(\Delta\theta)/\lambda$ .  $\theta$  and  $\lambda$  are the diffraction angle and the wavelength (0.015583989 nm) of synchrotron x-ray,  $\Delta\theta$  is the full width at half-maximum (FWHM) which is obtained by a Voigt fitting to experimental diffraction line profile using a Python script with LmFit package [39]. A modified Williamson-Hall approach [40,41] was used to assess the dislocation density, details of the analysis are presented in Supplementary data C.

To further visualize the extent of difference in dislocation density between the

deformed and the undeformed regions, a parameter ‘Relative Dislocation Density’ (RDD) was defined as:

$$RDD = \frac{DD-LDD}{LDD}, (2)$$

where LDD is the lowest dislocation density, which is assigned to the data point with greatest distance away from indentation, i.e. undeformed region.

## 2.7 Finite element modeling

The commercial finite element analysis (FEA) software, Abaqus, was used to simulate the residual stress and strain distribution after spherical indentation. To reduce computational cost, both the sample and indenter tip were assumed to be axially symmetric. Therefore, two-dimensional axially symmetric models were used [42]. Quadrilateral axisymmetric elements (CAX4R) were used to construct the finite element model, with fine enough meshes located around the indentation affected region to ensure the convergence of the simulation. By treating the sample as an elastic-plastic isotropic solid, the indentation process was simulated based on displacement control, with three steps considered according to the experimental condition, i.e., pre-loading, loading, and unloading. The simulation result was validated by comparing the indentation contact projection area and load-time curve with experimental data. The simulation details, including material properties, boundary conditions, and configurations and validations of the model, are provided in Supplementary data D.

## 2.8 Phase field simulation

A phase field grain growth model [43] was used to describe the recrystallization process after plastic deformation. The total energy of the system can be expressed as:

$$F(\eta_{i=0..k}) = \int \left( \sum_{i=0}^k \left( -\frac{a_1}{2} \eta_i^2 + \frac{a_2}{4} \eta_i^4 \right) + \frac{a_3}{2} \sum_{i,j=0..k}^{j \neq i} \eta_i^2 \eta_j^2 + \frac{\alpha}{2} \sum_{i=0}^k (\nabla \eta_i)^2 + \sum_{i=0}^k \varepsilon_i (\eta_i)^2 \right) dr^3, (3)$$

details of this formulation and phase field model are included in the Supplementary data E.

A 2D simulation cell with 1024 by 128 grids was used. The grid size was 0.4  $\mu\text{m}$ , which

leads to a system size of 409.6  $\mu\text{m}$  by 51.2  $\mu\text{m}$ . The simulation used periodic boundary conditions along the vertical direction and Neumann boundary conditions along the horizontal direction. An initial quench from the liquid state was simulated to create a fine equiaxed grain structure. The average grain area is  $\sim 13.8 \mu\text{m}^2$ , which corresponds to a grain diameter of 4.2  $\mu\text{m}$ . Small pinning precipitates were introduced which will not evolve (coarsening is not considered). The area fraction of the precipitates was 1.643% ( $\sim 190$  particles in the system), diameter of the precipitates is 1.6  $\mu\text{m}$ . A total of 144 grain orientations were considered in the simulation. The simulation cell was divided into four regions from top to bottom, such that in each region, there are at least 36 different orientations to prevent severe grain coalescence [43]. The grain boundary energy was set to 0.6 J/m<sup>2</sup>.

### 3. Results

#### 3.1. Microstructure observation

Prior to deformation and heat treatment, the as-extruded alloy is composed of uniform fine and equiaxed grains (Fig. 1a). The inverse polar figure (IPF) map confirms the absence of ALGs. The polar figure reveals a very weak texture with a maximum value of 1.52 mud (Multiples of a uniform density) based on the orientation distribution densities. Distribution densities with a maximum 1 mud represent perfectly uniform distribution of crystal orientation [44], i.e., no preferential texture. Previous investigation also revealed that negligible texture was found in PM nickel-based superalloys after HIP consolidation, hot extrusion or heat treatment [45,46]. Therefore, the effect of strong texture inhibition on grain growth could be ignored. The measurement of grain size distribution, Fig. 1(b), shows the average grain size is 2.39  $\mu\text{m}$  (finer than ASTM 14), with a maximum distribution frequency between 1 and 2  $\mu\text{m}$ . Under the mode of backscattered electron (BSE) image, Fig. 1(c), precipitates such as carbides and/or borides on the grain boundaries are evident and believed to play a critical role in inhibiting grain growth [2]. Primary  $\gamma'$  precipitates with a size range of 0.5-1  $\mu\text{m}$  are randomly

located on the grain boundaries based on the observation of secondary electron image, Fig. 1(d), while finer secondary  $\gamma'$  precipitates are embedded within  $\gamma$  grains [47].

To investigate the effect of deformation on grain size evolution, spherical indentation was applied to generate a deformed microstructure gradient, Fig. 2(a). Because of different deformation history, the plastic strain/stored energy/driving force used for grain evolution varies from location to location upon subsequent supersolvus heat treatments. Fig. 2(b-c) shows the grain structure close to the indentation impression after 5 min of supersolvus heat treatment. Specifically, the BSE micrograph of the indented plane, Fig. 2(b), reveals that ALGs occur in the region 0.5-1 mm away from the indentation center (Fig. 2(a-b)) in an annular manner. Viewing towards the cross section, the occurrence of ALGs is confined to a narrow band and a closer EBSD examination demonstrates that the size of an ALG is much larger than other grains, i.e., exceeding 200  $\mu\text{m}$ , Fig. 2(d).

### 3.2. Strain and dislocation density localization beneath the indentation impression

It is clear that ALGs occur in positions associated with the extent of deformation. However, it is quite challenging to experimentally measure the residual plastic strain, and hence, a validated FEM simulation was employed to quantify the value. Fig. 3 shows the contours of the plastic shear strain component ( $\epsilon_{12}^{pl}$ ) and the effective plastic strain ( $\epsilon_{\text{eff}}^{pl}$ ) after indentation. The effective plastic strain,  $\epsilon_{\text{eff}}^{pl}$ , is defined by  $\sqrt{\frac{2}{3}\epsilon^{pl}:\epsilon^{pl}}$ , where  $\epsilon^{pl}$  is the plastic strain tensor[48]. As shown in Fig. 3(a), the maximum plastic shear strain (29%) occurs at the circumference of the contact projection area where the surface of the indenter contacts with the sample material first during indentation and then forces the local material to flow away. However, the maximum effective plastic strain occurs in the material located at the center of the contact projection area and just beneath the indenter tip, as shown in Fig. 3(b). In addition, the iso-strain contour of the effective plastic strain indicates that the indentation-induced plastic

deformation region is in a semi-elliptical shape in the radial-axial plane.

It is well established that EBSD hit rate (percentage of data points successfully indexed) is positively correlated to the amount of deformation [49]. By measuring the EBSD hit rates, the amount of deformation was found to be strongly dependent on the distance to indentation impression (see Supplementary data F). The localized strain distribution was analyzed by local misorientation data in the area with high hit rate (92.52%) and where is the approximate position that ALGs can be found (Fig. 4). It can be seen that several grains in white circles have higher local misorientation values, Fig. 4(a), which indicates a higher extent of accumulated deformation. The local misorientation angle distribution of area corresponding to 0 mm, 0.7 mm and 1.25 mm to the indentation impression is shown in Fig. 4(b); the inset shows the area which is least deformed has a larger percentage of high misorientation angles distribution [50]. This indicates that small deformation induces more heterogeneous strain distribution.

Previously, several methods based on EBSD data [51,52] have been proposed to estimate geometrically necessary dislocation (GND) [53] density by correlating the GND distribution to lattice curvature in a physically based framework [53–55]. Yet, full dislocation density cannot be acquired because of the existence of statistically stored dislocation that is not related to the crystallographic misorientation. Herein, we employ synchrotron radiation technique to characterize the full dislocation density. Fig. 5(a) presents the contour of calculated dislocation density with respect to the indentation impression. The experimental result indicates gradient distribution of dislocation density in a semi-elliptical shape, which is in good agreement with the effective plastic strain contour, Fig. 3(d), rather than the shear plastic strain. The experimental measurement unambiguously demonstrates that the dislocation density has increased up to more than 20 times from the undeformed region to the severely plastic affected region, Fig. 5(b). The consistency from synchrotron measurement to effective

plastic strain further validates the FEM model.

### 3.3. Heat treatment response of indented samples

Based on the above results, an appropriate range of plastic strain and dislocation density is needed to trigger ALGs. In the following, we further characterize the role of annealing temperature and heating rate in affecting grain growth behavior of ALGs.

Fig. 6(a) is the microscopic observation of ALGs after experiencing supersolvus solution for 30s in the induction heated specimen, and ALGs occur in the region between ~800-1200  $\mu\text{m}$  under the indentation impression. In comparison, the region of ALGs occurrence diverges to ~1000 to 1700  $\mu\text{m}$  under the indentation impression when the annealing time is increased to 5 min, indicating continuous grain growth over time during supersolvus heat treatment. On the other hand, no visible ALGs are found in the specimen heat treated at subsolvus temperature for 5 min, Fig. 6(c). The difference can be attributed to the role of precipitates in inhibiting grain growth during subsolvus annealing. This further verifies the role of grain boundary precipitates in inhibiting grain growth. In powder metallurgy nickel-based superalloys, the primary  $\gamma'$  is dissolved under supersolvus solution and thus grain growth is permitted. In contrast, subsolvus solution treatment can restrain grain growth since the primary  $\gamma'$  is insoluble.

Based on the statistical results of EBSD grain size measurement, Fig. 6(d) shows the dependence of largest grain size as a function of the distance from the indentation impression. Upon supersolvus treatment, the largest grain size appears in the position from 960  $\mu\text{m}$  (the grain size is 180  $\mu\text{m}$ ) and 1193  $\mu\text{m}$  (the grain size is 208  $\mu\text{m}$ ) for 30 s and 5 min, respectively, corresponding to the observation in Fig. 6(a) and Fig. 6(b). It is noteworthy to point out that the largest grain size decreases slightly in the region from 800-1200  $\mu\text{m}$  upon subsolvus annealing. However, the metallurgical mechanism needs further research.

Fig. 6(e) shows the dislocation density and effective plastic strain (the variable PEMAG

in Abaqus is chosen to display this result) value in the critical region where ALG was observed, i.e., 800-1800  $\mu\text{m}$  under the indentation impression. The value of RDD ranges from 10.07 to 3.22, which corresponds to a dislocation density from  $1.16 \times 10^{15} \text{ m}^{-2}$  to  $4.42 \times 10^{14} \text{ m}^{-2}$ . Similarly, the effective plastic strain changes in the range from 8.6% to 1.8%. For the specimen upon 30 s supersolvus annealing, the RDD and effective plastic strain at the peak position of ALG grain size are 8.6 (dislocation density:  $1 \times 10^{15} \text{ m}^{-2}$ ) and 6.8%, respectively. When the annealing time is increased to 5 min, the values change to 6.4 (dislocation density:  $7.7 \times 10^{14} \text{ m}^{-2}$ ) and 4.7%, respectively.

Fig. 7 illustrates the evolution of ALGs under the condition of supersolvus annealing with different times from 35s to 5 hr. It can be observed that the regions of ALGs occurrence overlap irrespective of the longer annealing time, indicating the formation of ALGs is a fast process. A close-up view discloses that prolonged annealing time can drive preferential growth of ALGs towards the region with lower residual plastic strain (indicated by white arrows), leading to the formation of elongated grains.

Fig. 8 is an IPF map showing the ALGs distribute discontinuously in the matrix, implying only a few grains can grow abnormally at the very early stage. The grain boundaries of these ALGs are tortuous and concave towards the grain interior. In this regard, there is a driving force available for ALG growth by means of consuming surrounding fine grains [56]. It is interesting to point out that a high density of twinning can be observed in the fine grains situated near the grain boundary of ALGs.

#### 4. Discussion

According to both experimental and simulation results, residual plastic strain (von Mises or effective plastic strain) is directly related to dislocation density  $\rho$ , Fig. 6(e). From the classic work of Kocks et al. [57,58], the stored energy from dislocation can be estimated as:

$$\text{stored energy} = \alpha \mu b^2 \rho \ln \frac{R_e}{b}, \quad (4)$$

where  $\alpha$  is a parameter depending on dislocation type,  $\mu$  is the shear modulus,  $b$  is the Burgess vector and  $R_e$  is the effective outer cutoff radius of dislocations. Therefore, the stored energy could be correlated to dislocation density, as well as residual plastic strain. In this study, ALGs were found only in the supersolvus heat treated samples in a critical region with relatively low residual plastic strain ranging from ~2% to ~10%, i.e. in a critical range of stored energy. Unimodal grain size distribution was observed in the region with both high stored energy and substantially low stored energy after supersolvus heat treatment.

#### 4.1 Phase field simulation study

To further understand the effect of stored energy on the formation of ALGs, a phase field simulation was conducted to capture grain growth behavior in the polycrystalline model with different stored energy.

Different levels of stored energy were added into the model, Fig. 9(a), the lowest quarter (Region 1) had no added stored energy, the second quarter (Region 2) had stored energy:  $0.2085 \times 10^6 \text{ J/m}^3$ , the third quarter (Region 3):  $0.417 \times 10^6 \text{ J/m}^3$  (double as much as Region 2) and the fourth quarter (the upper most) (Region 4):  $0.6255 \times 10^6 \text{ J/m}^3$  (triple as much as Region 2). These values were chosen according to the work of Agnoli et al. [26]. The color contrast in Fig. 9 indicates the amount of stored energy: red being no stored energy, while orange to yellow indicates increasing stored energy. The simulated results are shown in Fig. 9 for 4 different scenarios.

##### **Scenario 1, Fig. 9(b), recrystallization is inhibited:**

If no recrystallization is allowed, only NGG is assumed and similar grain size distribution is produced in all four regions, the driving force is capillary force,  $P_C$ . One interesting feature is that there are elongated grains at the boundary of the regions, where a sharp gradient of stored energy exists, the grains with low stored energy grow towards the region with high stored energy as suggested by the strain induced boundary migration (SIBM)



mechanism [59]. The driving force is stored energy difference across grain boundary,  $P_{SE}$ . It can be also confirmed by the color contrast, that the produced large and elongated grains are with less stored energy than the neighbor grains in the same region.

#### **Scenario 2, Fig. 9(c), recrystallization is allowed:**

Now, nuclei of recrystallized grains are introduced periodically by randomly putting new grains without stored energy on the grain boundary. The diameter of the new grains is set to be  $1.6\ \mu\text{m}$ . However, if the new grain is introduced at the region with low or no stored energy (Region 1 and 2), it will quickly shrink and disappear. Only when the neighboring grains have relatively high stored energy, can the new grain be stabilized and grow. Small recrystallized grains can be seen in the upper most region (region 4) because of the high stored energy. With many stable new grains, they quickly overtake the whole region and consume all grains with high stored energy and then impinge on each other. Region 3 has fewer stable new grains because of the lower stored energy. So, these grains have more room to grow before impingement. This results in very coarse grains. Region 2 has a small stored energy, which is not able to stabilize new grains, thus, it can only be gradually overtaken by the growth of grains without strain from neighboring regions. It also can be found in Region 2, if no recrystallization process happens, the stored energy remains relatively stable.

#### **Scenario 3, Fig. 9(d), high volume fraction of pinning particles is added:**

The initial state of Scenario 3 has the same stored energy as in Scenario 2, but higher volume fraction of pinning particles (area fraction  $\sim 3.6\%$ ), Fig. 9(d). The diameter of the precipitates is still set to be  $1.6\ \mu\text{m}$ . The very coarse grains appear in the same region 3 as in scenario 2 but the overall grain size is smaller due to the higher pinning pressure,  $P_Z$ , exerted by the higher fraction of pinning particles

#### **Scenario 4, Fig. 9(e), with increased stored energy in all regions:**

If we double the stored energy for all the regions (the lowermost quarter still has 0 added stored energy), regions 3 and 4 are quickly saturated with newly recrystallized grains and the growth of those new grains impinge on each other. Region 2 ends up with large grains as fewer recrystallized grains are stabilized which have more room to grow.

To capture more details of the grain growth process, the evolution of microstructure with different simulation time which correspond to Scenario 2 is shown in Fig. 10. It can be seen that at a later stage, the coarse grains in Region 3 tend to grow in the direction of lower stored energy in Region 2.

#### **4.2. Formation mechanism of ALGs**

In the results section, ALGs region, Fig. 8, occurs at the location with low dislocation density, Fig. 6. This is direct evidence to show that the occurrence of ALGs is a stored energy driven phenomenon. Thus, abnormal grain growth (AGG) mechanism alone cannot account for the ALGs in the present study, because the main driving force for AGG is capillarity in order to minimize grain boundary energy. Besides, the ALG front velocity in the present investigation ( $5.1 \mu\text{m/s}$ ), similar to a previous investigation [3], is considerably faster than what the AGG predicts [3]. With further consideration, if AGG starts in a reasonable uniform alloy containing pinning particles in which NGG cannot take place by retardation effect on grain boundary migration, then abnormal grains will grow at no hindrance because the neighbour boundaries are pinned by particles and become immobile. The growth of abnormal grains will make them have size advantage to its neighbour grains, which in turn have more driving force to grow [60]. So it is unlikely that AGG would start and just stop. This did is not happened in this investigation as indicated in Fig. 8 that ALGs region also has stopped at a lower bound. This would also provide a plausible evidence that growth of ALGs is not AGG.

If no recrystallization occurs in all the regions to change the stored energy distribution, a smooth stored energy gradient could exist. As indicated by Scenario 1, Fig. 9(b), in the phase field study, the simulated microstructure after annealing could be anticipated as slightly elongated grains, and it is unlike the observed ALGs. So, it is reasonable to assume that recrystallization occurs during supersolvus heat treatment. It has been proposed [10] and indicated by Scenario 2 in phase field study, that only nuclei with (1) high local misorientation to adjacent deformed matrix and (2) an energy advantage could be stabilized and later grow into recrystallized grains until mutual impingement. Otherwise, the nuclei could shrink or vanish into the matrix. Thus, the final recrystallized grain size depends on active nucleation sites.

Fig. 11 schematically summarizes the grain growth mechanisms in different regions underneath the indentation. Adjacent to the surface, strain was highly localized at a high level ( $>10\%$ ). A large number of nucleation sites for recrystallization could be easily initiated and later stabilized in this high stored energy-contained region, thus producing a unimodal grain size distribution. The stored energy in this region has been significantly consumed by recrystallization process and then decreased.

In the region with substantially low stored energy (below  $\sim 2\%$  residual plastic strain), the driving force is **insufficient inadequate** for recrystallization even by the strain induced boundary migration (SIBM) mechanism. Thus, it is assumed that only recovery and normal grain growth could take place in this region, and unimodal grain size could be produced.

In the region further away from the indentation impression with medium strain ( $2\%-10\%$ ) hence lower stored energy, ALGs are found after annealing. Two possible mechanisms can be both attributed to the initiation stage of ALG as described in the introduction section: (1) nucleation limited recrystallization and (2) heterogeneity of store energy distribution at an intragranular scale. Firstly, the density of stable nuclei is statistically much less due to the

decrease of stored energy in microstructure, compared to the higher strain region below the indentation impression. The few nuclei could be stabilized in the deformed matrix and later grow into ALGs at the expense of neighboring grains until mutual impingement. Additionally, the nucleation of ALGs could be most likely attributed to the SIBM mechanism at small strains [59]. This involves the migration of pre-existing grain boundaries into the adjacent deformed matrix, leaving a region with less dislocation content behind the migrated boundary [6]. The driving force of this kind of grain boundary migration is the stored energy difference across the grain boundary. Therefore, a heterogeneous distribution of stored energy at intragranular scale could have a great impact on SIBM process. The stored energy distribution is thought to be anisotropic in grain scale in the polycrystalline alloy, considering a wide spread of orientations [61]. Thus, some grains might contain higher stored energy after deformation due to the orientation dependent hardening behavior than its peers nearby (as indicated by Fig. 4), which can be absorbed by neighboring grains with lower stored energy and then grow into ALGs.

The growth of ALGs, can be driven by both capillary force and SIBM mechanism. When nucleation of ALGs is completed, the stored energy in nuclei is reduced and can grow into neighboring grains which still contain some extent of stored energy assisted by capillary force due to size advantage. At a later stage, the ALGs tend to grow into lower strained regions (further away from the indentation impression), in which stored energy has not been largely consumed by recrystallization. This could be confirmed by experimental observation in Fig. 7 and phase field simulation in Fig. 10.

In order to release stored energy, the remaining grains in the matrix other than ALGs in the critical region undergo realignment of atomic structure process by SIBM as well [62]. This process is accompanied by formation of annealing twins [63,64], as shown in Fig. 8(b), triggered by the interaction of dissociated dislocation with mobile grain boundaries [65]. Thus, the existence of many fine grains with a high density of annealing twins in the critical region

could be an indicator that SIBM has happened.

### **Conclusions:**

Strain gradient was induced by spherical indentation in a PM nickel-based superalloy. The contour lines of effective (von Mises) plastic strain obtained by FEM simulation, correlate to the contours of dislocation density measured by synchrotron diffraction.

ALGs (Abnormally Large Grains) are only found in supersolvus heat treated samples, and in the region with residual plastic strain level of ~2%-10%. Thus, the ALGs only occur in a critical range of stored energy. Similarity between the outline of ALGs region and the contour lines of dislocation density has been found. This indicates the formation of ALGs is driven by stored energy distribution since the stored energy and dislocation density in deformed microstructure could be positively correlated. The formation of ALGs are proposed to be an abnormal recrystallization process with limited stable nuclei, which are most likely nucleated by the SIBM (Strain Induced Boundary Migration) mechanism. The heterogeneous distribution of stored energy across grain boundary at ALGs nucleation sites is thought to **be** have a big impact on this SIBM process. After the limited nucleation of ALGs is completed, ALGs grow at the expense of neighboring grains until mutual impingement. This process is governed by capillary force and SIBM mechanism. At the final stage of growth, ALGs tend to grow into lower strained regions, and the growth finally stagnates at a critical value of strain.

On the contrary, in the high stored energy region, a fine grain size distribution is maintained by static recrystallization, and the recrystallization process is not limited by the number of active nucleation sites. In the very low stored energy region, the driving force of static recrystallization is low enough, only normal grain growth exists.

This research provides a deeper understanding of the formation mechanism of ALGs during heat treatment in polycrystalline nickel-based superalloy components, **when subsurface**

plastic deformation caused by (mis)handling before super-solvus heat treatment occurs. Producing turbine disks involves ~~in~~ a series of thermo-mechanical processing at high temperatures. In particular for the isothermal forging, ~~in between~~, the forging parameters must be carefully chosen to maintain the superplastic deformation. If not, the excessive stored energy could be stored in the workpieces, which induces the growth of ALGs ~~abnormal grain growth~~ during subsequent heat treatment [66]. In addition, the near net shape forging could lead to more severe deformation localization and dead zone near surface, which triggers ALGs in the interior of the part. Our method using indentation-and-annealing is not directly related to the high temperature forging process but provide some aspects to understand the formation mechanism of ALGs in forging workpieces.

#### **Acknowledgement:**

Prof. Liang Jiang and Prof. Zaiwang Huang appreciate the financial support from the National Key Research and Development Program of China (2016YFB0700300). Xin Wang appreciates the support from the outstanding graduate project of Advanced Non-ferrous Metal Structural Materials and Manufacturing Collaborative Innovation Center. Suggestions from Prof. Yunzhi Wang of The Ohio State University and Yikai Wang of University of Kentucky are also acknowledged. Authors thank Prof. Hui Yang of Huazhong University of Science and Technology for revising the manuscript.

## References

- [1] G.H. Gessinger, M.J. Bomford, Powder Metallurgy of Superalloys, International Metallurgical Reviews. 19 (1974) 51–76.
- [2] D.M. Collins, B.D. Conduit, H.J. Stone, M.C. Hardy, G.J. Conduit, R.J. Mitchell, Grain growth behaviour during near- $\gamma'$  solvus thermal exposures in a polycrystalline nickel-base superalloy, Acta Mater. 61 (2013) 3378–3391.
- [3] V.M. Miller, A.E. Johnson, C.J. Torbet, T.M. Pollock, Recrystallization and the Development of Abnormally Large Grains After Small Strain Deformation in a Polycrystalline Nickel-Based Superalloy, Metall. Mater. Trans. A. 47 (2016) 1566–1574.
- [4] T.P. Gabb, P.T. Kantzos, J. Telesman, J. Gayda, C.K. Sudbrack, B. Palsa, Fatigue resistance of the grain size transition zone in a dual microstructure superalloy disk, Int. J. Fatigue. 33 (2011) 414–426.
- [5] J. Miao, T.M. Pollock, J. Wayne Jones, Crystallographic fatigue crack initiation in nickel-based superalloy René 88DT at elevated temperature, Acta Mater. 57 (2009) 5964–5974.
- [6] F.J. Humphreys, M. Hatherly, Recrystallization and Related Annealing Phenomena, Elsevier, 2012.
- [7] T. Gladman, N.P. Allen, On the theory of the effect of precipitate particles on grain growth in metals, Proc. R. Soc. Lond. A Math. Phys. Sci. 294 (1966) 298–309.
- [8] J.J. Bhattacharyya, S.R. Agnew, G. Muralidharan, Texture enhancement during grain growth of magnesium alloy AZ31B, Acta Mater. 86 (2015) 80–94.
- [9] W.E. Frazier, G.S. Rohrer, A.D. Rollett, Abnormal grain growth in the Potts model incorporating grain boundary complexion transitions that increase the mobility of individual boundaries, Acta Mater. 96 (2015) 390–398.
- [10] R.D. Doherty, D.A. Hughes, F.J. Humphreys, J.J. Jonas, D.J. Jensen, M.E. Kassner, W.E. King, T.R. McNelley, H.J. McQueen, A.D. Rollett, Current issues in recrystallization: a

- review, *Materials Science and Engineering: A*. 238 (1997) 219–274.
- [11] M. Hillert, On the theory of normal and abnormal grain growth, *Acta Metall.* 13 (1965) 227–238.
- [12] P.R. Rios, Abnormal grain growth development from uniform grain size distributions, *Acta Mater.* 45 (1997) 1785–1789.
- [13] F.J. Humphreys, A unified theory of recovery, recrystallization and grain growth, based on the stability and growth of cellular microstructures—II. The effect of second-phase particles, *Acta Mater.* 45 (1997) 5031–5039.
- [14] I. Andersen, Ø. Grong, N. Ryum, Analytical modelling of grain growth in metals and alloys in the presence of growing and dissolving precipitates—II. Abnormal grain growth, *Acta Metall. Mater.* 43 (1995) 2689–2700.
- [15] I. Andersen, Ø. Grong, Analytical modelling of grain growth in metals and alloys in the presence of growing and dissolving precipitates—I. Normal grain growth, *Acta Metall. Mater.* 43 (1995) 2673–2688.
- [16] D.A. DeMania, Recovery and recrystallization in nickel-based superalloy René 88 DT, University of Virginia, 2002.
- [17] C.P. Blankenship Jr, M.F. Henry, J.M. Hyzak, R.B. Rohling, E.L. Hall, Hot-Die Forging of P/M Ni-Base Superalloys, in: *Superalloys 1996 (Eighth International Symposium)*, TMS, 1996: pp. 653–662.
- [18] M. Dahlen, L. Winberg, Grain coarsening of PM nickel-base superalloy by critical strain annealing, *Met. Sci. Heat Treat.* 13 (1979) 163–169.
- [19] C.P. Blankenship Jr., W.T. Carter Jr., A.E. Murut, M.F. Henry, Recrystallization and grain growth in strain gradient samples, *Scripta Metallurgica et Materialia*. 31 (1994) 647–652.
- [20] M. Soucail, M. Marty, H. Octor, The Effect of High Temperature Deformation on Grain Growth in a PM Nickel Base Superalloy, in: 1996: pp. 663–666.



- [21] E. Huron, S. Srivatsa, E. Raymond, Control of Grain Size Via Forging Strain Rate Limits for Rene88DT, in: Superalloys 2000 (Ninth International Symposium), TMS, 2000: pp. 49–58.
- [22] Y.K. Cho, D.Y. Yoon, M.F. Henry, The effects of deformation and pre-heat-treatment on abnormal grain growth in RENÉ 88 superalloy, *Metall. Mater. Trans. A.* 32 (2001) 3077–3090.
- [23] D.D. Whitis, Recovery and Recrystallization After Critical Strain in the Nickel-Based Superalloy Rene’ 88DT, in: Superalloys 2004 (Tenth International Symposium), TMS, 2004: pp. 391–400.
- [24] T.P. Gabb, J. Gayda, J. Falsey, Forging of Advanced Disk Alloy LSHR, 2005.
- [25] S.L. Semiatin, J.M. Shank, A.R. Shiveley, W.M. Saurber, E.F. Gaussa, A.L. Pilchak, The Effect of Forging Variables on the Supersolvus Heat-Treatment Response of Powder-Metallurgy Nickel-Base Superalloys, *Metall. Mater. Trans. A.* 45 (2014) 6231–6251.
- [26] A. Agnoli, M. Bernacki, R. Logé, J.-M. Franchet, J. Laigo, N. Bozzolo, Selective Growth of Low Stored Energy Grains During  $\delta$  Sub-solvus Annealing in the Inconel 718 Nickel-Based Superalloy, *Metall. Mater. Trans. A.* 46 (2015) 4405–4421.
- [27] O.D. Underwood, J.D. Madison, G.B. Thompson, Emergence and Progression of Abnormal Grain Growth in Minimally Strained Nickel-200, *Metals* . 7 (2017) 334.
- [28] I.M.D. Parr, T.J. Jackson, M.C. Hardy, D.J. Child, C. Argyrakis, K. Severs, V. Saraf, J.M. Stumpf, Inhomogeneous Grain Coarsening Behavior in Supersolvus Heat Treated Nickel-Based Superalloy RR1000, in: Superalloys 2016, John Wiley & Sons, Inc., 2016: pp. 447–456.
- [29] M.-A. Charpagne, J.-M. Franchet, N. Bozzolo, Overgrown grains appearing during sub-solvus heat treatment in a polycrystalline  $\gamma$ - $\gamma'$  Nickel-based superalloy, *Mater. Des.* 144 (2018) 353–360.

- [30] A. Agnoli, M. Bernacki, R. Logé, J. Franchet, J. Laigo, N. Bozzolo, Understanding and Modeling of Grain Boundary Pinning in Inconel 718, in: Superalloys 2012 (Twelfth International Symposium), John Wiley & Sons, Inc., 2012: pp. 73–82.
- [31] W. Tu, T.M. Pollock, Grain Scale Straining Processes during High Temperature Compression of a PM Disk Alloy, in: Superalloys 2008 (Eleventh International Symposium), TMS, 2008: pp. 395–403.
- [32] W.J. Tu, Deformation mechanisms and strain storage during forging of powder-metallurgy nickel-base turbine disk alloy, University of Michigan, 2010.
- [33] L. Tan, Z. Huang, F. Liu, G. He, X. Wang, L. Huang, Y. Zhang, L. Jiang, Effects of strain amount and strain rate on grain structure of a novel high Co nickel-based polycrystalline superalloy, *Mater. Des.* 131 (2017) 60–68.
- [34] J.E. Burke, D. Turnbull, Recrystallization and grain growth, *Prog. Phys. Met. / Uspehi Fiziki Metallov.* 3 (1952) 220–292.
- [35] C. Zambaldi, F. Roters, D. Raabe, U. Glatzel, Modeling and experiments on the indentation deformation and recrystallization of a single-crystal nickel-base superalloy, *Materials Science and Engineering: A.* 454-455 (2007) 433–440.
- [36] C.-Z. Liu, F. Liu, L. Huang, L. Jiang, Effect of hot extrusion and heat treatment on microstructure of nickel-base superalloy, *Trans. Nonferrous Met. Soc. China.* 24 (2014) 2544–2553.
- [37] G.K. Williamson, W.H. Hall, X-ray line broadening from filed aluminium and wolfram, *Acta Metall.* 1 (1953) 22–31.
- [38] T. Ungár, A. Borbély, The effect of dislocation contrast on x-ray line broadening: A new approach to line profile analysis, *Appl. Phys. Lett.* 69 (1996) 3173–3175.
- [39] M. Newville, T. Stensitzki, D.B. Allen, A. Ingargiola, LMFIT: Non-Linear Least-Square Minimization and Curve-Fitting for Python, 2014. doi:10.5281/zenodo.11813.

- [40] W. Woo, T. Ungár, Z. Feng, E. Kenik, B. Clausen, X-Ray and Neutron Diffraction Measurements of Dislocation Density and Subgrain Size in a Friction-Stir-Welded Aluminum Alloy, *Metall. Mater. Trans. A*. 41 (2010) 1210–1216.
- [41] G. Ribárik, T. Ungár, J. Gubicza, A. Borbély, Crystallite size distribution and dislocation structure determined by diffraction profile analysis: principles and practical application to cubic and hexagonal crystals, *J. Appl. Crystallogr.* 34 (2001) 298–310.
- [42] Y. Wang, Y.-T. Cheng, A nanoindentation study of the viscoplastic behavior of pure lithium, *Scr. Mater.* 130 (2017) 191–195.
- [43] D. Fan, L.-Q. Chen, Computer simulation of grain growth using a continuum field model, *Acta Mater.* 45 (1997) 611–622.
- [44] L.E. Watt, P.A. Bland, D.J. Prior, S.S. Russell, Fabric analysis of Allende matrix using EBSD, *Meteorit. Planet. Sci.* 41 (2006) 989–1001.
- [45] M. Detrois, Grain boundary engineering of powder-processed Ni-base superalloy RR1000, Illinois Institute of Technology, 2016.
- [46] J. Xu, Z. Huang, L. Jiang, Low cycle fatigue behavior of a high Co polycrystalline nickel-base superalloy at 750 °C, *J. Alloys Compd.* 749 (2018) 1106–1114.
- [47] D. Scott MacKenzie, G.E. Totten, Analytical Characterization of Aluminum, Steel, and Superalloys, Taylor & Francis, 2005.
- [48] Hibbitt, Karlsson, Sorensen, ABAQUS: Theory manual, Hibbitt, Karlsson & Sorensen, 1997.
- [49] A.J. Wilkinson, T.B. Britton, Strains, planes, and EBSD in materials science, *Mater. Today*. 15 (2012) 366–376.
- [50] S.I. Wright, M.M. Nowell, D.P. Field, A review of strain analysis using electron backscatter diffraction, *Microsc. Microanal.* 17 (2011) 316–329.
- [51] E. Demir, D. Raabe, N. Zaafarani, S. Zaefferer, Investigation of the indentation size effect

- through the measurement of the geometrically necessary dislocations beneath small indents of different depths using EBSD tomography, *Acta Mater.* 57 (2009) 559–569.
- [52] T.B. Britton, H. Liang, F.P.E. Dunne, A.J. Wilkinson, The effect of crystal orientation on the indentation response of commercially pure titanium: experiments and simulations, *Proceedings of the Royal Society A: Mathematical, Physical and Engineering Sciences.* 466 (2010) 695–719.
- [53] M.F. Ashby, The deformation of plastically non-homogeneous materials, *The Philosophical Magazine: A Journal of Theoretical Experimental and Applied Physics.* 21 (1970) 399–424.
- [54] J.F. Nye, Some geometrical relations in dislocated crystals, *Acta Metall.* 1 (1953) 153–162.
- [55] E. Kröner, On the plastic deformation of polycrystals, *Acta Metall.* 9 (1961) 155–161.
- [56] W.W. Mullins, Two-Dimensional Motion of Idealized Grain Boundaries, *J. Appl. Phys.* 27 (1956) 900–904.
- [57] U.F. Kocks, R.O. Scattergood, Elastic interactions between dislocations in a finite body, *Acta Metall.* 17 (1969) 1161–1168.
- [58] G. Mohamed, B. Bacroix, Role of stored energy in static recrystallization of cold rolled copper single and multicrystals, *Acta Mater.* 48 (2000) 3295–3302.
- [59] P.A. Beck, P.R. Sperry, Strain Induced Grain Boundary Migration in High Purity Aluminum, *J. Appl. Phys.* 21 (1950) 150–152.
- [60] E.A. Holm, T.D. Hoffmann, A.D. Rollett, C.G. Roberts, Particle-assisted abnormal grain growth, *IOP Conf. Ser.: Mater. Sci. Eng.* 89 (2015) 012005.
- [61] B. Bacroix, R. Brenner, A phenomenological anisotropic description for dislocation storage and recovery processes in fcc crystals, *Comput. Mater. Sci.* 54 (2012) 97–100.
- [62] M. Detrois, J. McCarley, S. Antonov, R.C. Helmink, R.L. Goetz, S. Tin, Comparative

study of high-temperature grain boundary engineering of two powder-processed low stacking-fault energy Ni-base superalloys, *Mater. High Temp.* 33 (2016) 310–317.

[63] Y. Jin, B. Lin, M. Bernacki, G.S. Rohrer, A.D. Rollett, N. Bozzolo, Annealing twin development during recrystallization and grain growth in pure nickel, *Materials Science and Engineering: A*. 597 (2014) 295–303.

[64] N. Bozzolo, N. Souaï, R.E. Logé, Evolution of microstructure and twin density during thermomechanical processing in a  $\gamma$ - $\gamma'$  nickel-based superalloy, *Acta Mater.* 60 (2012) 5056–5066.

[65] J. McCarley, S. Tin, Utilization of hot deformation to trigger strain induced boundary migration (SIBM) in Ni-base superalloys, *Materials Science and Engineering: A*. 720 (2018) 189–202.

[66] D.D. Krueger, R.D. Kissinger, R.G. Menzies, C.S. Wukusick, Fatigue crack growth resistant nickel-base article and alloy and method for making, 4957567, 1990.

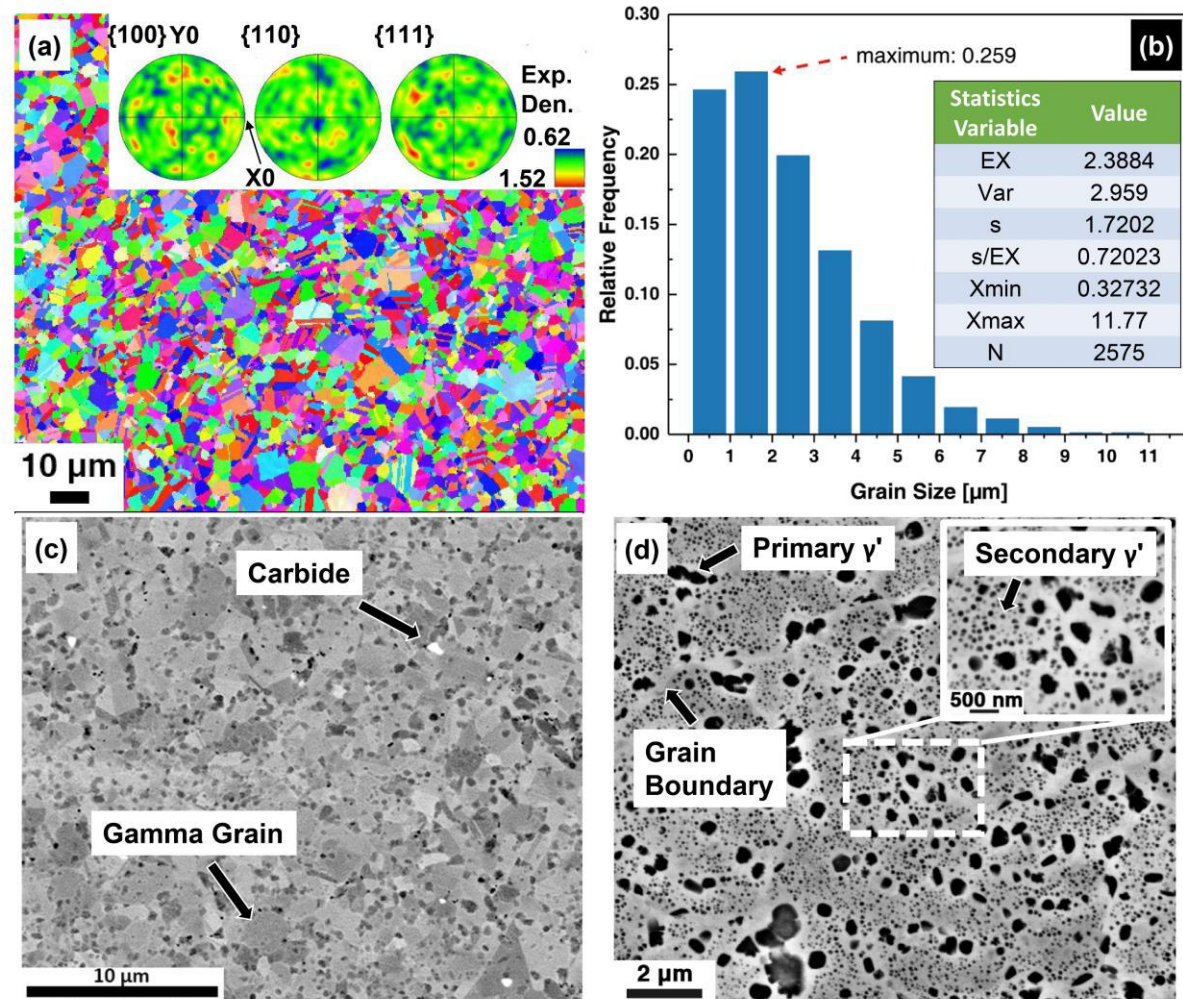


Fig. 1. Microstructure of as-extruded material. (a) IPF map showing uniform distribution of grain size and no preferential texture. (b) Grain size distribution statistics indicating a unimodal grain size distribution. (c) BSE image showing carbides and borides. (d) SE image illustrating two distinct gamma prime precipitates.

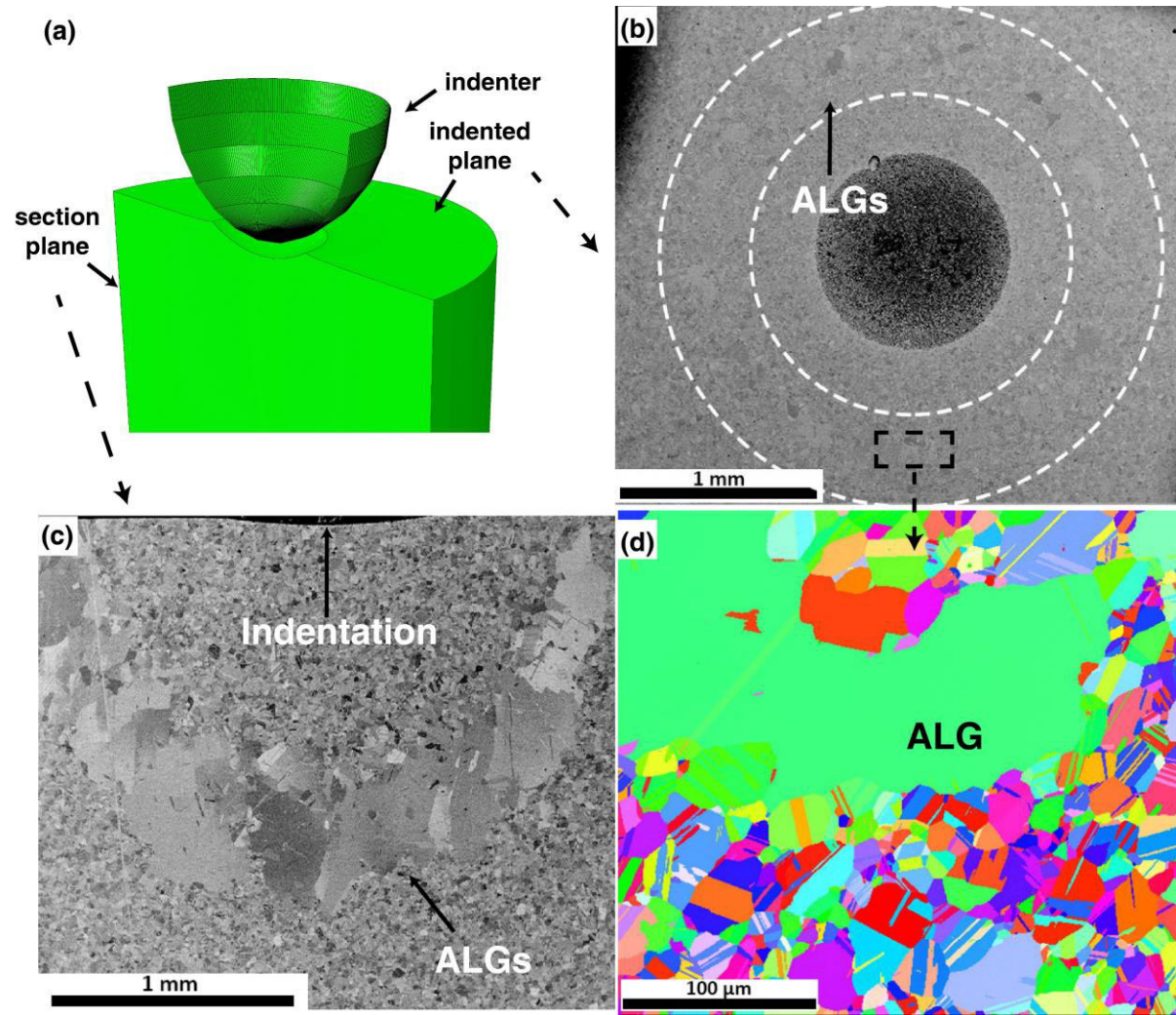


Fig. 2. Schematic graph of occurrence of ALGs in the sample after supersolvus heat treatment for 5 min. (a) Configuration of indentation experiment. (b) ALGs appears in a circular manner in the indented plane. (c) ALGs grain appears in a semi-elliptical manner in the section plane. (e) IPF map of a selected area from Fig. 5(b) which shows the length of an ALG intercept could be over 200  $\mu\text{m}$ .



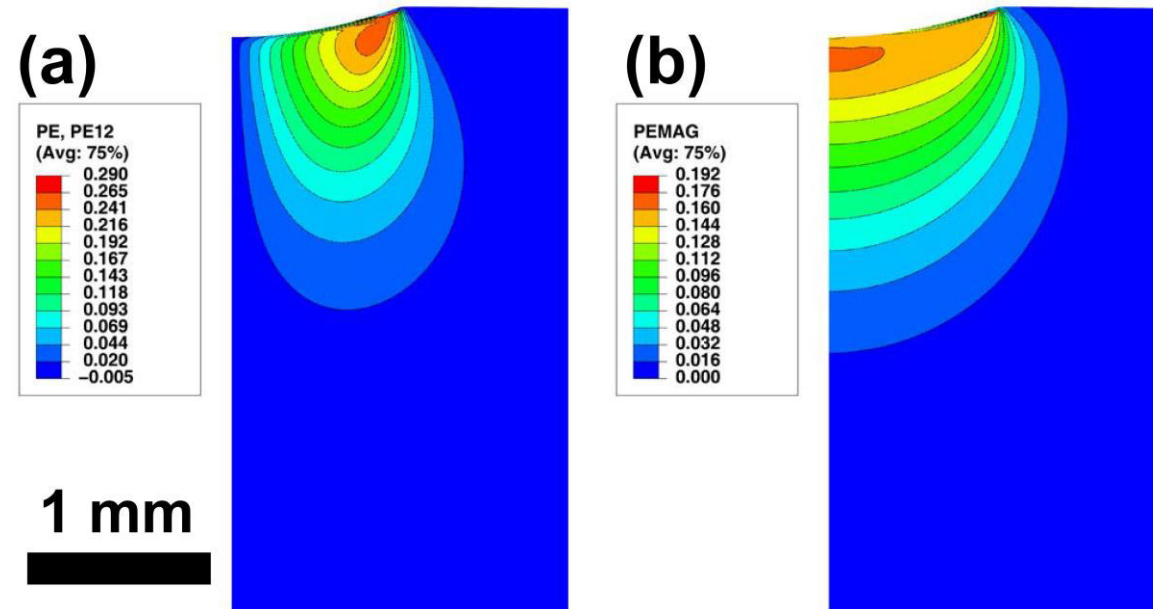


Fig. 3. FEM simulation results with different residual plastic strain indicator: (a) PE12 (shear strain component); (b) Effective plastic strain.



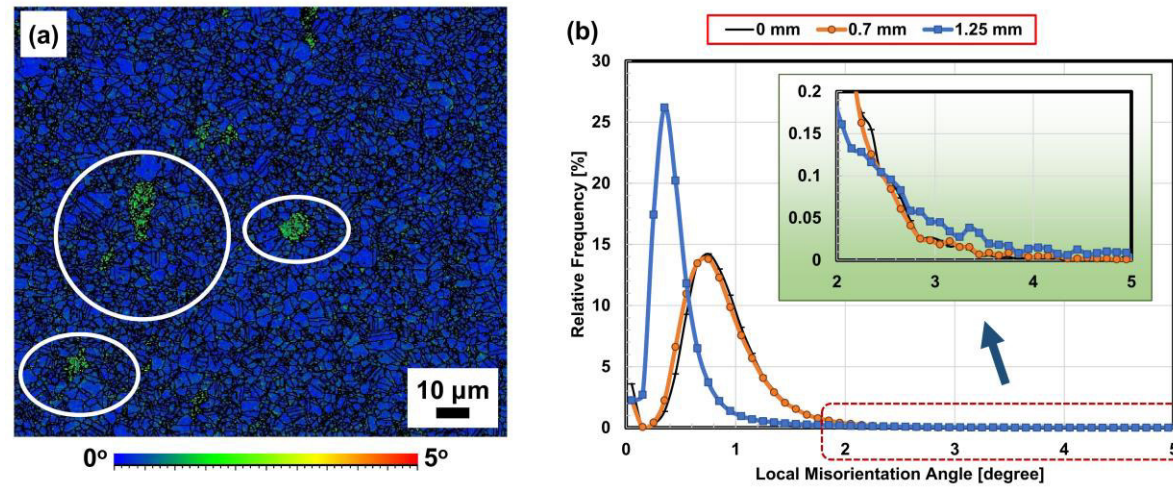


Fig. 4. Local misorientation analysis of the indented sample. (a) Local misorientation map with center of acquisition area 1.25 mm away from indentation. Grains in white circles have higher value of local misorientation, indicating inhomogeneous accumulation of deformation. (b) Local misorientation angle distribution of area corresponding to Fig. 3(a)-(c), enlarged graph shows the area which is 1.25 mm away from indentation has a larger percentage of high misorientation angle distribution.

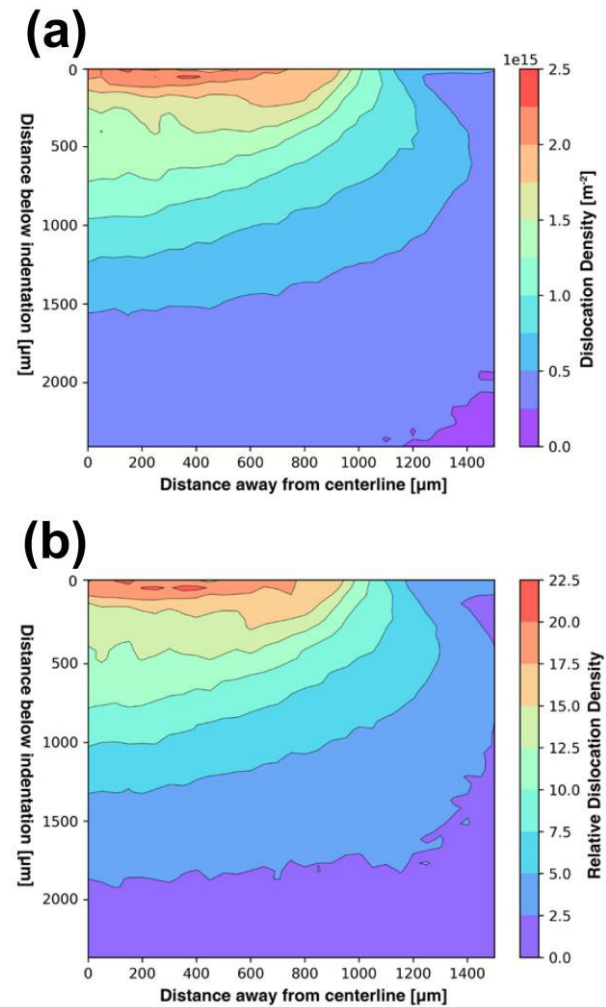


Fig. 5. Contour plots of the dislocation density caused by indentation. Dislocation density contours under indentation. (a) Dislocation density contours. (b) Relative dislocation density contours indicating the degree of dislocation increases from undeformed region.

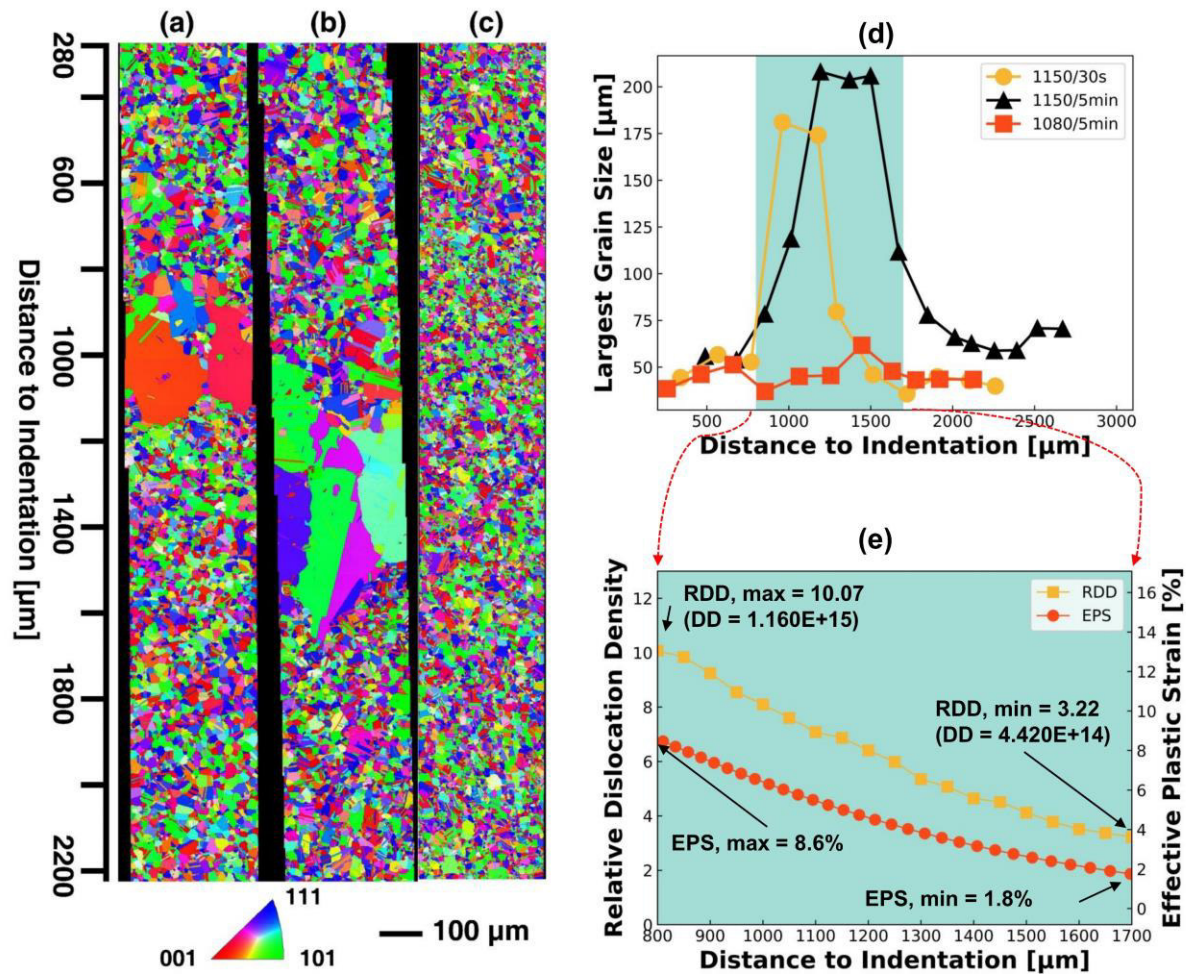


Fig. 6. Different heat treatment response. (a) IPF of **HH**-induction heating sample. (b) IPF map of the sample heat treated at 1150 °C for 5 min. (c) IPF map of the sample heat treated at 1080 °C for 5 min. (d) Relationship between ALA grain size and distance to indentation of three samples under different heat treatment conditions, showing the location of ALGs. (e) Plot of dislocation density and effective plastic strain value against distance to indentation in the ALGs region. RDD: relative dislocation density; EPS: effective plastic strain

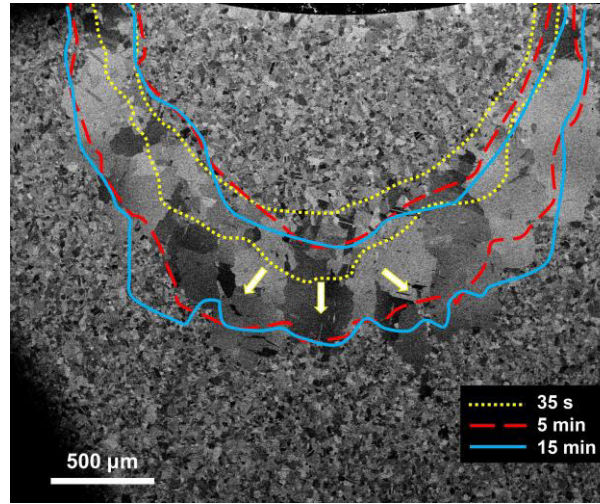


Fig. 7. BSD image showing the appearance of ALGs in the sample heat treated at 1150 °C for 5 hours with ALGs appearance of sample heat treated at 1150 °C for 35s, 5 min and 15 min outlined.



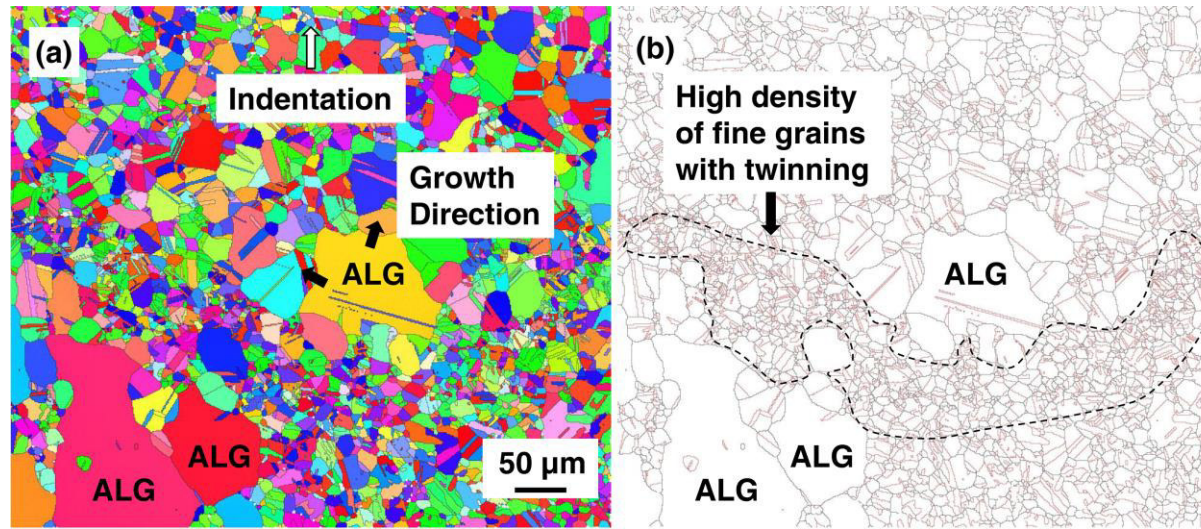


Fig. 8. An enlarged view of the critical region of **HH**-induction heating sample. (a) IPF map showing the ALGs occur in a discrete manner with concave grain boundaries. (b) Grain boundaries map with twin boundaries showing high density of fine grains with twin boundaries appears in the middle of ALGs.

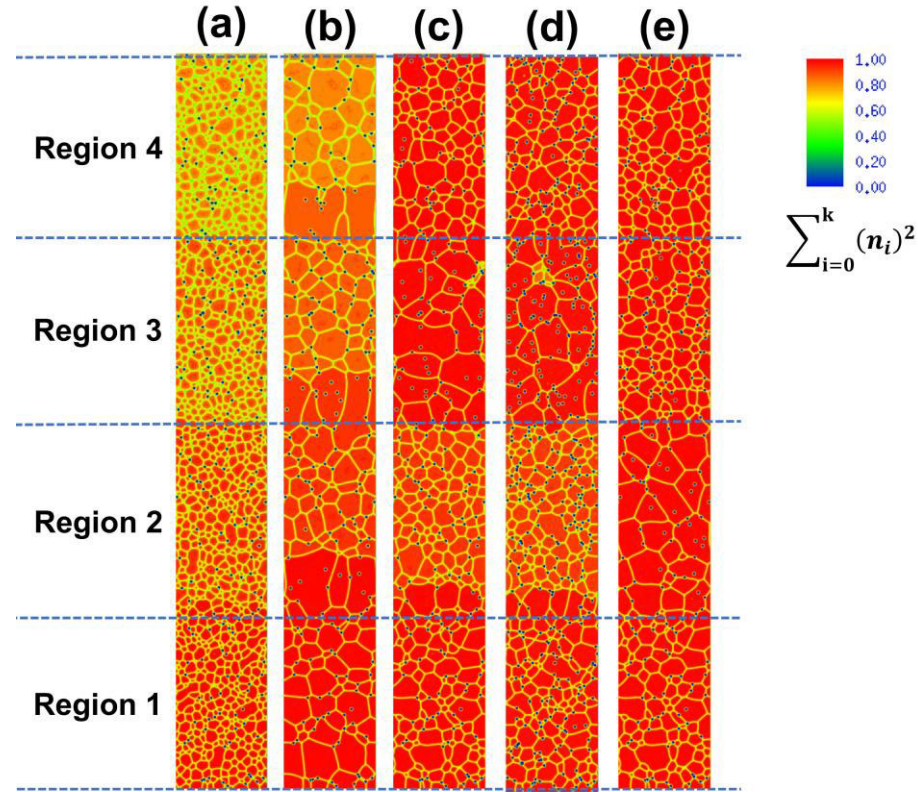


Fig. 9. Phase field simulation results, the color scale is based on sum of squared order parameter,  $\sum_{i=0}^k (n_i)^2$ , detailed information of this scale bar has been added in the supplementary data E. (a) Initial configuration with different SE (stored energy) added separately in region 1: no SE added; region 2:  $0.2085 \times 10^6 \text{ J/m}^3$ ; region 3:  $0.417 \times 10^6 \text{ J/m}^3$  and region 4:  $0.6255 \times 10^6 \text{ J/m}^3$ ; red background indicates there is no residual SE (b) No recrystallization is allowed, and only columnar grains appear in the region boundaries with sharp stored energy (c) Recrystallization is allowed and very large grains appear in region 3 with moderate stored energy. (d) With increase of pinning particles, very coarse grains appear in the same region 3 as scenario 2 but the overall grain size is smaller. (e) After doubling the stored energy in each region, coarse grains appear in region 2.

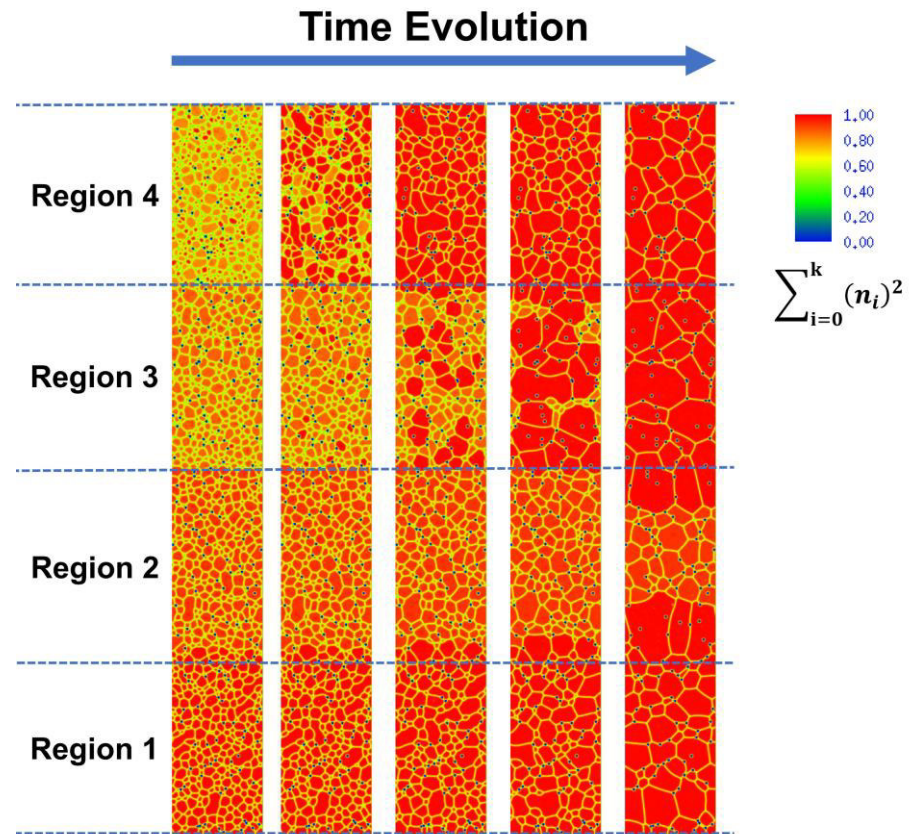


Fig. 10. Evolution of microstructure with time corresponding to Fig. 9(c)



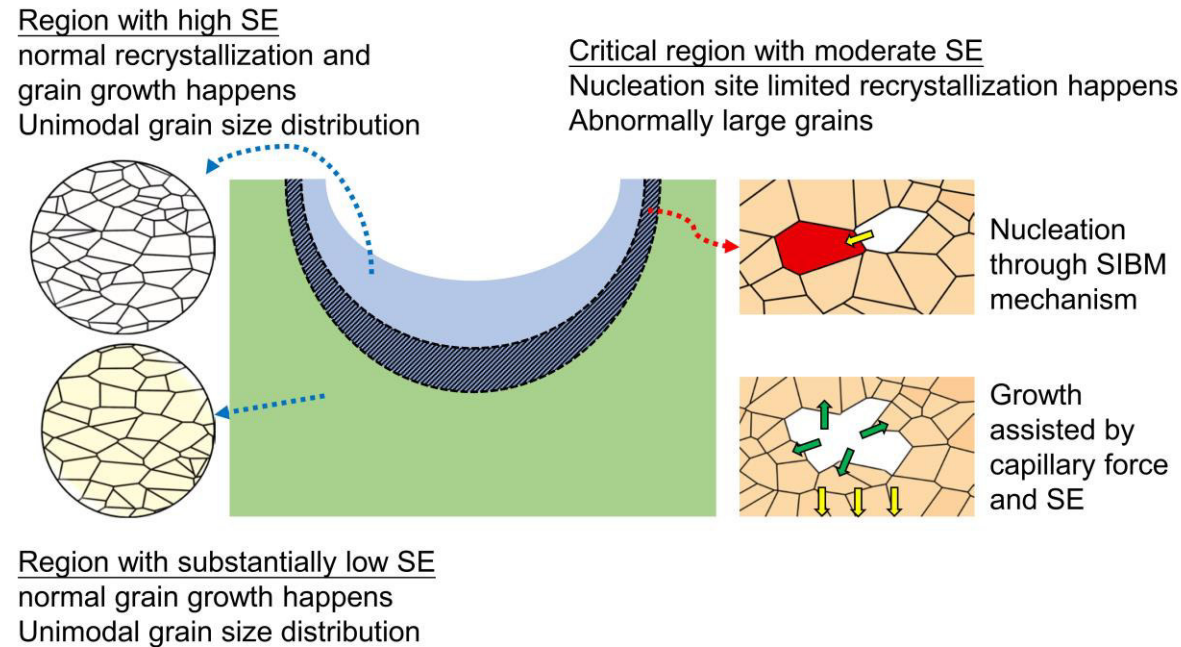


Fig. 11. Schematic diagram of formation mechanism of ALGs. Normal recrystallization and grain growth process happen in the region with high SE (stored energy), thus produce an unimodal grain size distribution due to large number of nucleation sites. Nucleation site limited recrystallization happens in the critical region, the nucleation of limited nuclei is by SIBM mechanism. The growth of ALGs is assisted by SE and capillary force. In the region with substantially low SE, only NGG normal grain growth process take place thus produce an unimodal grain size distribution.